Research Article | Vol. 25, No. 18 | 4 Sep 2017 | OPTICS EXPRESS 20953
Optics EXPRESS

Divide and update: towards single-shot object and probe retrieval for near-field holography

JOHANNES HAGEMANN[1,2] AND TIM SALDITT[1,3]

[1]*Universität Göttingen, Institut für Röntgenphysik, Friedrich-Hund-Platz 1, 37077 Göttingen Germany*
[2]*jhagema@gwdg.de*
[3]*tsaldit@gwdg.de*

Abstract: We present a phase reconstruction scheme for X-ray near-field holographic imaging based on a separability constraint for probe and object. In order to achieve this, we have devised an algorithm which requires only two measurements – with and without an object in the beam. This scheme is advantageous if the standard flat-field correction fails and a full ptychographic dataset can not be acquired, since either object or probe are dynamic. The scheme is validated by numerical simulations and by a proof-of-concept experiment using highly focused undulator radiation of the beamline ID16a of the European Synchrotron Radiation Facility (ESRF).

OCIS codes: (340.7440) X-ray imaging; (100.5070) Phase retrieval; (180.7460) X-ray microscopy.

References and links

1. D. Gabor, "Theory of communication," J. Instn. Elect. Engrs. **93**, 429–457 (1946).
2. A. Snigirev, I. Snigireva, V. Kohn, S. Kuznetsov, and I. Schelokov, "On the possibilities of x-ray phase contrast microimaging by coherent high-energy synchrotron radiation," Rev. Sci. Instrum. **66**, 5486–5492 (1995).
3. A. Rack, M. Scheel, L. Hardy, C. Curfs, A. Bonnin, and H. Reichert, "Exploiting coherence for real-time studies by single-bunch imaging," J. Synchrotron Rad. **21**, 815–818 (2014).
4. A. Schropp, R. Hoppe, V. Meier, J. Patommel, F. Seiboth, Y. Ping, D. G. Hicks, M. A. Beckwith, G. W. Collins, A. Higginbotham, J. S. Wark, H. J. Lee, B. Nagler, E. C. Galtier, B. Arnold, U. Zastrau, J. B. Hastings, and C. G. Schroer, "Imaging shock waves in diamond with both high temporal and spatial resolution at an xfel," Sci. Rep. **5**, 11089 (2015).
5. P. Kirkpatrick and A. V. Baez, "Formation of Optical Images by X-Rays," J. Opt. Soc. Am. **38**, 766–773 (1948).
6. J. Hagemann, A.-L. Robisch, M. Osterhoff, and T. Salditt, "Probe reconstruction for holographic X-ray imaging," J. Synchrotron Rad. **24**, 498–505 (2017).
7. R. Horisaki, Y. Ogura, M. Aino, and J. Tanida, "Single-shot phase imaging with a coded aperture," Opt. Lett. **39**, 6466 (2014).
8. P. Tafforeau, R. Boistel, E. Boller, A. Bravin, M. Brunet, Y. Chaimanee, P. Cloetens, M. Feist, J. Hoszowska, and J.-J. Jaeger, "Applications of x-ray synchrotron microtomography for non-destructive 3d studies of paleontological specimens," Appl. Phys. A **83**, 195–202 (2006).
9. B. D. Metscher, "Biological applications of x-ray microtomography: imaging microanatomy, molecular expression and organismal diversity," Microsc Anal (Am Ed) **27** (2013).
10. T. van de Kamp, P. Vagovič, T. Baumbach, and A. Riedel, "A biological screw in a beetle's leg," Science **333**, 52–52 (2011).
11. J. Moosmann, A. Ershov, V. Altapova, T. Baumbach, M. S. Prasad, C. LaBonne, X. Xiao, J. Kashef, and R. Hofmann, "X-ray phase-contrast in vivo microtomography probes new aspects of xenopus gastrulation," Nature **497**, 374–377 (2013).
12. C. Homann, T. Hohage, J. Hagemann, A.-L. Robisch, and T. Salditt, "Validity of the empty-beam correction in near-field imaging," Phys. Rev. A **91**, 013821 (2015).
13. J. Hagemann, A.-L. Robisch, D. R. Luke, C. Homann, T. Hohage, P. Cloetens, H. Suhonen, and T. Salditt, "Reconstruction of wave front and object for inline holography from a set of detection planes," Opt. Express **22**, 11552–11569 (2014).
14. S. Hoffmann-Urlaub, P. Höhne, M. Kanbach, and T. Salditt, "Advances in fabrication of x-ray waveguides," Microelectron. Eng. **164**, 135–138 (2016).
15. M. Osterhoff and T. Salditt, "Coherence filtering of x-ray waveguides: analytical and numerical approach," New J. Phys. **13**, 103026 (2011).
16. M. Krenkel, A. Markus, M. Bartels, C. Dullin, F. Alves, and T. Salditt, "Phase-contrast zoom tomography reveals precise locations of macrophages in mouse lungs," Sci. Rep. **5**, 09973 (2015).
17. M. Bartels, M. Krenkel, J. Haber, R. N. Wilke, and T. Salditt, "X-ray holographic imaging of hydrated biological cells in solution," Phys. Rev. Lett. **114**, 048103 (2015).

#296808 https://doi.org/10.1364/OE.25.020953
Journal © 2017 Received 26 May 2017; revised 28 Jul 2017; accepted 28 Jul 2017; published 21 Aug 2017

Optics EXPRESS

18. M. Töpperwien, M. Krenkel, K. Müller, and T. Salditt, "Phase-contrast tomography of neuronal tissues: from laboratory-to high resolution synchrotron ct," Proc. SPIE **9967**, 99670T (2016).
19. O. Bunk, M. Dierolf, S. Kynde, I. Johnson, O. Marti, and F. Pfeiffer, "Influence of the overlap parameter on the convergence of the ptychographical iterative engine," Ultramicroscopy **108**, 481–487 (2008).
20. P. Thibault, M. Dierolf, A. Menzel, O. Bunk, C. David, and F. Pfeiffer, "High-Resolution Scanning X-ray Diffraction Microscopy," Science **321**, 379–382 (2008).
21. J. Rodenburg, "Ptychography and Related Diffractive Imaging Methods," Adv. Imaging Electron Phys. **150**, 87–184 (2008).
22. A.-L. Robisch and T. Salditt, "Phase retrieval for object and probe using a series of defocus near-field images," Opt. Express **21**, 23345–23357 (2013).
23. M. Stockmar, I. Zanette, M. Dierolf, B. Enders, R. Clare, F. Pfeiffer, P. Cloetens, A. Bonnin, and P. Thibault, "X-ray near-field ptychography for optically thick specimens," Phys. Rev. Applied **3**, 014005 (2015).
24. P. Thibault and A. Menzel, "Reconstructing state mixtures from diffraction measurements," Nature **494**, 68–71 (2013).
25. J. Hagemann and T. Salditt, "Reconstructing mode mixtures in the optical near-field," Opt. Express **25**, 13973–13989 (2017).
26. J. Hagemann and T. Salditt, "The fluence–resolution relationship in holographic and coherent diffractive imaging," J. Appl. Crystallogr. **50**, 531–538 (2017).
27. R. Neutze, R. Wouts, D. van der Spoel, E. Weckert, and J. Hajdu, "Potential for biomolecular imaging with femtosecond X-ray pulses," Nature **406**, 752–757 (2000).
28. H. N. Chapman, A. Barty, M. J. Bogan, S. Boutet, M. Frank, S. P. Hau-Riege, S. Marchesini, B. W. Woods, S. Bajt, W. H. Benner, R. A. London, E. Plonjes, M. Kuhlmann, R. Treusch, S. Dusterer, T. Tschentscher, J. R. Schneider, E. Spiller, T. Moller, C. Bostedt, M. Hoener, D. A. Shapiro, K. O. Hodgson, D. van der Spoel, F. Burmeister, M. Bergh, C. Caleman, G. Huldt, M. M. Seibert, F. R. N. C. Maia, R. W. Lee, A. Szoke, N. Timneanu, and J. Hajdu, "Femtosecond diffractive imaging with a soft-X-ray free-electron laser," Nat. Phys. **2**, 839–843 (2006).
29. H. N. Chapman, P. Fromme, A. Barty, T. A. White, R. A. Kirian, A. Aquila, M. S. Hunter, J. Schulz, D. P. DePonte, U. Weierstall, R. B. Doak, F. R. N. C. Maia, A. V. Martin, I. Schlichting, L. Lomb, N. Coppola, R. L. Shoeman, S. W. Epp, R. Hartmann, D. Rolles, A. Rudenko, L. Foucar, N. Kimmel, G. Weidenspointner, P. Holl, M. Liang, M. Barthelmess, C. Caleman, S. Boutet, M. J. Bogan, J. Krzywinski, C. Bostedt, S. Bajt, L. Gumprecht, B. Rudek, B. Erk, C. Schmidt, A. Homke, C. Reich, D. Pietschner, L. Struder, G. Hauser, H. Gorke, J. Ullrich, S. Herrmann, G. Schaller, F. Schopper, H. Soltau, K.-U. Kuhnel, M. Messerschmidt, J. D. Bozek, S. P. Hau-Riege, M. Frank, C. Y. Hampton, R. G. Sierra, D. Starodub, G. J. Williams, J. Hajdu, N. Timneanu, M. M. Seibert, J. Andreasson, A. Rocker, O. Jonsson, M. Svenda, S. Stern, K. Nass, R. Andritschke, C.-D. Schroter, F. Krasniqi, M. Bott, K. E. Schmidt, X. Wang, I. Grotjohann, J. M. Holton, T. R. M. Barends, R. Neutze, S. Marchesini, R. Fromme, S. Schorb, D. Rupp, M. Adolph, T. Gorkhover, I. Andersson, H. Hirsemann, G. Potdevin, H. Graafsma, B. Nilsson, and J. C. H. Spence, "Femtosecond X-ray protein nanocrystallography," Nature **470**, 73–77 (2011).
30. J. M. J. Madey, "Stimulated emission of bremsstrahlung in a periodic magnetic field," J. Appl. Phys. **42**, 1906–1913 (1971).
31. P. Thibault, M. Dierolf, A. Menzel, O. Bunk, C. David, and F. Pfeiffer, "High-Resolution Scanning X-ray Diffraction Microscopy: Supporting online material," Science **321**, 379–382 (2008).
32. T. Osaka, M. Yabashi, Y. Sano, K. Tono, Y. Inubushi, T. Sato, S. Matsuyama, T. Ishikawa, and K. Yamauchi, "A bragg beam splitter for hard x-ray free-electron lasers," Opt. Express **21**, 2823–2831 (2013).
33. W. Roseker, H. Franz, H. Schulte-Schrepping, A. Ehnes, O. Leupold, F. Zontone, S. Lee, A. Robert, and G. Grübel, "Development of a hard X-ray delay line for X-ray photon correlation spectroscopy and jitter-free pump–probe experiments at X-ray free-electron laser sources," J. Synchrotron Rad. **18**, 481–491 (2011).
34. J. Hagemann and T. Salditt, "Divide and update: Towards single-shot object and probe retrieval for near-field holography: Algorithm and simulation scripts," https://doi.org/10.5281/zenodo.838005 (2017).
35. K. Giewekemeyer, S. P. Krüger, S. Kalbfleisch, M. Bartels, C. Beta, and T. Salditt, "X-ray propagation microscopy of biological cells using waveguides as a quasipoint source," Phys. Rev. A **83**, 023804 (2011).
36. D. R. Luke, "Relaxed Averaged Alternating Reflections for Diffraction Imaging," Inverse Prob. **21**, 37 (2005).
37. M. V. Heel, "Angular reconstitution: A posteriori assignment of projection directions for 3d reconstruction," Ultramicroscopy **21**, 111–123 (1987).
38. M. van Heel and M. Schatz, "Fourier shell correlation threshold criteria," J. Struct. Biol. **151**, 250–262 (2005).
39. A.-L. Robisch, J. Wallentin, A. Pacureanu, P. Cloetens, and T. Salditt, "Holographic imaging with a hard x-ray nanoprobe: ptychographic versus conventional phase retrieval," Opt. Lett. **41**, 5519–5522 (2016).
40. G. Kutyniok, W.-Q. Lim, and R. Reisenhofer, "Shearlab 3d: Faithful digital shearlet transforms based on compactly supported shearlets," ACM Trans. Math. Softw. **42**, 5:1–5:42 (2016).
41. S. Loock and G. Plonka, "Phase retrieval for fresnel measurements using a shearlet sparsity constraint," Inverse Probl. **30**, 055005 (2014).
42. A. Pein, S. Loock, G. Plonka, and T. Salditt, "Using sparsity information for iterative phase retrieval in x-ray propagation imaging," Opt. Express **24**, 8332–8343 (2016).
43. M. Stockmar, P. Cloetens, I. Zanette, B. Enders, M. Dierolf, F. Pfeiffer, and P. Thibault, "Near-field ptychography: phase retrieval for inline holography using a structured illumination," Sci. Rep. **3**, 1927 (2013).

Optics EXPRESS

44. M. Stockmar, M. Hubert, M. Dierolf, B. Enders, R. Clare, S. Allner, A. Fehringer, I. Zanette, J. Villanova, J. Laurencin, P. Cloetens, F. Pfeiffer, and P. Thibault, "X-ray nanotomography using near-field ptychography," Opt. Express **23**, 12720–12731 (2015).
45. A.-L. Robisch, K. Kröger, A. Rack, and T. Salditt, "Near-field ptychography using lateral and longitudinal shifts," New J. Phys. **17**, 073033 (2015).
46. P. Thibault, V. Elser, C. Jacobsen, D. Shapiro, and D. Sayre, "Reconstruction of a yeast cell from X-ray diffraction data," Act. Cryst. A **62**, 248–261 (2006).
47. G. Kutyniok, D. Labate, W.-Q. Lim, M. Leitheiser, R. Reisenhofer, and X. Zhuang, "Shearlab," http://www.shearlab.org/ (2017).
48. S. Mallat, *A Wavelet Tour of Signal Processing: The Sparse Way* (Academic Press, 2008), 3rd ed.

1. Introduction

X-ray near-field holographic imaging (NFH) enables single shot, full-field imaging of specimen with nanoscale spatial resolution [1, 2]. Sharing the characteristic advantages of high penetration and quantitative contrast with other x-ray imaging modalities, it can in addition exploit the advantage of high temporal resolution down to single pulse imaging with synchrotron (SR) and free electron laser (FEL) radiation [3, 4]. This is for the simple reason, that a full wavefield can be probed in a single shot without scanning. Figure 1 depicts the setup of NFH using highly focused SR or FEL radiation. By choice of the source to object distance z_1 and the object to detector distance z_2, the geometric magnification $M = (z_2 + z_1)/z_1$ and the field of view (FOV) can be tailored to the experimental need.

A major challenge in NFH is the fact that the validity of phase retrieval and hence image quality depends crucially on the quality of the illumination. Due to the finite source-size, a number of unwanted effects can arise, such as distortions in the wavefront or a partial coherent illumination, but also geometrical optical effects such as astigmatism. For example, focusing by elliptically shaped multilayer mirrors in Kirkpatrick-Baez geometry [5] is accompanied by unwanted phase distortions in the incoming X-ray probe induced by deviations from the ideal height profile of the mirrors [6]. After free space propagation to the imaging or detection plane, the phase errors result in a measurable intensity pattern, which often appears as pronounced horizontal and vertical stripes due to the two orthogonal mirrors, see Fig. 2 for an example of an empty beam pattern. In other types of focusing similar distortions arise. Focusing is required to generate the diverging illumination for high magnification and resolution. Note that also for parallel beam propagation imaging it is extremely common to implicitly assume perfect plane wave illumination by performing the conventional flat-field correction [3, 7–11]. In previous studies, we have shown that under these conditions the commonly used standard flat-field correction, i.e. the division of measured intensities with the specimen in the beam by measured intensities without specimen in the beam, induces artifacts [12, 13], as illustrated in Fig. 2(c). To overcome these problems, the experimentalist can choose between two principal strategies: (i) corrections by a refined optical system (hardware), or (ii) corrections by enhanced algorithms (software). The hardware solution can consists in the simplest case by additional apertures to cut off typical intensity tails in the focal plane. A more sophisticated solution is the use of x-ray waveguides (WG) [14], which act as coherence and wavefront filters [15], providing improved illumination schemes for NFH [16–18]. This advantage comes at the cost of a reduced photon flux, and increased acquisition time. The algorithmic approach by ptychography, on the other hand, solves the flat-field problem by a precise reconstruction of the complex-valued illumination. In the language of ptychography the illumination is called the probe P. To this end multiple exposures of the specimen, or in ptychographic terms of the object O, are acquired at different transveral positions in the beam. This position scanning is extensive, since an overlap between 60% to 85% is necessary for proper convergence of the ptychographic algorithm [19], depending on experimental modalities. This applies for the far-field [20, 21] case of ptychography and its extensions to NFH [22, 23]. Ptychography can

Optics EXPRESS

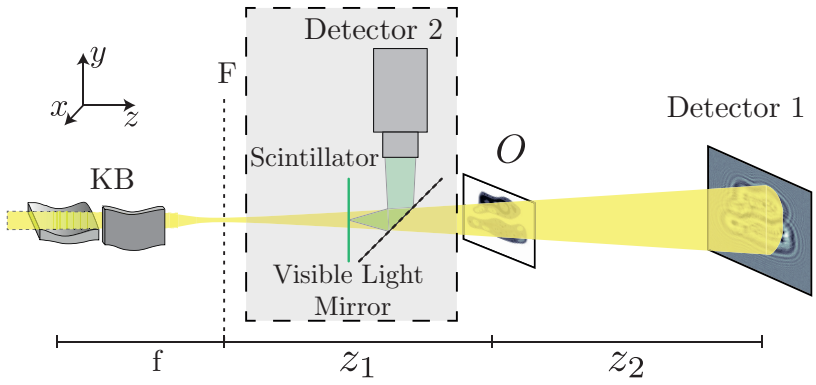

Fig. 1. Schematic of an experimental setup for near-field holography. Near-field holographic images are recorded with detector 1 at distance z_2 behind the object O, mounted on a motorized stage in defocus position z_1 behind the focal plane F of a Kirkpatrick-Baez mirror (KB) system with focal distance f. The dashed box shows the extension to a parallel acquisition setup. The two measurements $|\mathcal{D}_{\mathrm{Fr}}(\Psi)|^2$ and $|\mathcal{D}_{\mathrm{Fr}}(P)|^2$ can be acquired in single-shot by the use of a semi-transparent second detector. This Detector 2 is positioned front of O to record the illuminating probe. This experimental geometry is proposed for single-pulse FEL full field imaging scheme. For further discussions refer to the main text.

also account for other non ideal states (e.g. lack of coherence) of the probe or object [24, 25]. Associated with longer scanning time is also a larger data set, which has to be acquired by transversal and/or longitudinal (for the near-field) scans of O in order to generate sufficiently diverse input data for the simultaneous reconstruction of P and O. The scanning also imposes a higher dose on O, compared to NFH [26], which can induce radiation damage and lead to an inconsistent ptychographic dataset. Most importantly, the scanning scheme is incompatible with time-resolved studies and with ultra-fast (single shot) imaging. Note that some objects are deliberately destroyed by the first pulse, using the 'diffract-before-destroy' strategy used in some schemes of FEL imaging [27–29]. A further problem for ptychography at FEL is the intrinsic shot-to-shot variation of P, resulting from pulse generation by the SASE process [30].

In this work we seek to make single shot NFH compatible with non-stationary probes and in particular FEL imaging. To this end, we propose a new algorithmic approach. The reconstruction of object and probe is based on two intensity recordings: (i, exit wave) of the object in the beam and (ii, probe) of the empty beam without object. The exit wave $\Psi = P \cdot O$ is written as separable product of P and O. This implies that the product approximation holds, this is in general true for thin and especially biological specimen [31]. The proposed algorithm uses the separability constraint known from ptychography, and an intertwinded update scheme operating on both images, which we denote by divide&update (d&u), see Fig. 3. We show by simulation and experimentally that d&u yields an improved reconstruction quality of O compared to a reconstruction obtained from the same data using the standard flat-field correction as data preprocessor. The two images can be recorded either sequentially or simultaneously (parallel recording). As the probe stability was sufficiently high in the SR experiment serving as proof-of-concept in this work, we have used the sequential recording which is easier since no special detection scheme is necessary. In the case of parallel recording as required for single pulse FEL imaging, a semi-transparent detector screen in front of the object (denoted by detector 2 in Fig. 1) could be used, or a beam splitter in front of O to split the XFEL pulse before it interacts with O [32, 33].

Optics EXPRESS

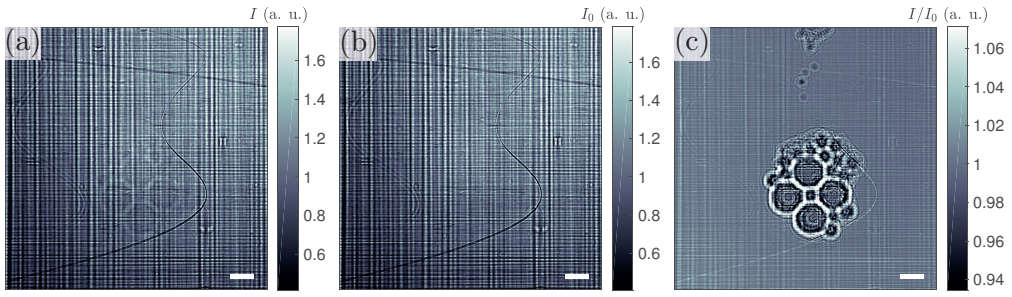

Fig. 2. Experimental data used for phase retrieval by d&u. (a) Recorded near-field intensity pattern with the object in the beam, i.e. $|\mathcal{D}_{\mathrm{Fr}}(\Psi)|^2$. (b) Same without object, i.e. $|\mathcal{D}_{\mathrm{Fr}}(P)|^2$. For comparison we also show (c) the flat-field correction of the object's hologram as obtained by dividing $|\mathcal{D}_{\mathrm{Fr}}(\Psi)|^2$ by $|\mathcal{D}_{\mathrm{Fr}}(P)|^2$. The scale bar indicates 5 µm.

For this purpose, a semi-transparent detection screen or beam splitter has to be placed in front of the object. There are two challenges to consider: Firstly, the sensor resolution has to sample the probe sufficiently well. Secondly, the heat load for the semi-transparent screen must be kept at a reasonable level. Both are difficult, if the detection screen is to close to the focal plane of a nano-focus optic. However, the 'probe detector' can equally well be placed in the convergent beam, e.g. directly behind the focusing device where the beam is extended, and where a field of view of several hundred micrometer could be probed with sufficient spatial sampling. In this case, the reconstruction requires additional propagation of the wavefields by Fresnel propagators, as also demonstrated in this work for simulated data in App. A.

The paper is structured as follows: Section 2 details the d&u scheme. Section 3 tests the algorithm on simulated data, before application to experimental data. The paper closes with summary and outlook in Sec. 4.

2. Algorithm

As in other ptychographic approaches, the d&u algorithm uses the separability constraint in the plane of O. Figure 3 shows a principle sketch of d&u and Algorithm 1 details the algorithmic approach. In conventional NFH, when dealing with distorted probes the approximative hologram of O [12] is recovered by flat-field correction and then used as input for a phase reconstruction algorithm. In contrast to this standard approach we make use of the two available measurements in an iterative reconstruction scheme, cf. Fig. 3. Following the separability idea of ptychography we use amplitude adapted version $\widehat{P_n} = \Pi_M^P(P_{n-1})$, $\widehat{\Psi}$ analogously, to yield updates for P_n and O_n in a cross-over manner (middle) by use of constraints for O in the plane of the object. With the new P_n and O_n we generate the updated exit wave Ψ and start a new iteration.

The projection on the measurements $\Pi_M^{\mathcal{X}}(\bullet)$, with $\mathcal{X}$ being either $|\mathcal{D}_{\mathrm{Fr}}(\Psi)|^2$ or $|\mathcal{D}_{\mathrm{Fr}}(P)|^2$, i.e. the respectively measured near field pattern, is given by the standard magnitude projector

$$\Pi_M^{\mathcal{X}}(\bullet) \equiv \mathcal{D}_{\mathrm{Fr}}{-1}\left(\mathcal{X}^{1/2} \cdot \exp\left(i \cdot \arg\left[\mathcal{D}_{\mathrm{Fr}}(\bullet)\right]\right)\right), \tag{1}$$

applied to the respective iterate of P or Ψ. The propagation to the detection plane is performed by the Fresnel free space propagator

$$\mathcal{D}_{\mathrm{Fr}}(\bullet) = \mathcal{F}^{-1}\left[\mathcal{F}\left[\bullet\right]\exp\left((-i\pi)/(2\,\mathrm{Fr})(k_x^2 + k_y^2)\right)\right], \tag{2}$$

where $k_x = 2\,n_x/N_x$ and $k_y = 2\,n_y/N_y$ are spatial frequencies in Fourier space with $n_{x,y} \in$

Optics EXPRESS

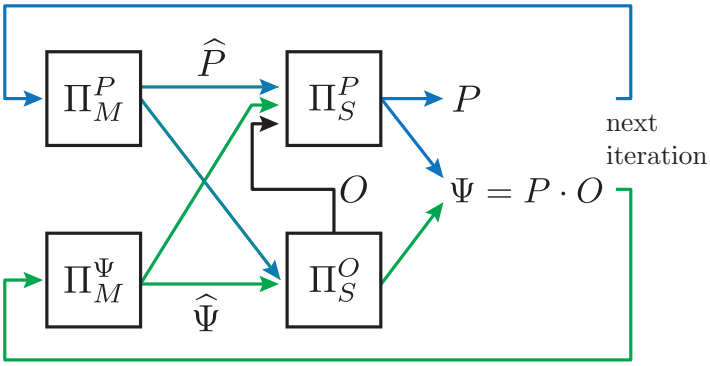

Fig. 3. Sketch of the algorithmic scheme of divide&update (d&u. The algorithm uses the two measurements $|\mathcal{D}_{\mathrm{Fr}}(\Psi)|^2$ and $|\mathcal{D}_{\mathrm{Fr}}(P)|^2$ as inputs. An iteration starts with the projection of the guesses for P and Ψ on the measured intensities using the projectors Π_M^P and Π_M^Ψ (left). After projection, the output fields $\widehat{P}$ and $\widehat{\Psi}$ are used in a cross-over manner to update P and O in Π_S^O and Π_S^P (middle), which are then multiplied to form the Ψ for the next iteration (right).

$\left[-N_{x,y}/2 \ldots N_{x,y}/2\right]$, $N_{x,y}$ are the dimensions of the image, $\mathcal{F}$ the Fourier transformation and Fr is the Fresnel number with respect to one pixel (px).

Algorithm 1 Divide and Update algorithm

1:	$O_0 \leftarrow \mathbb{1}_{N_x \times N_y}$	▷ Initialization
2:	$P_0 \leftarrow \mathbb{1}_{N_x \times N_y}$	
3:	**for** $n = 1 \ldots n_{max}$ **do**	
4:	$\widehat{P_n} \leftarrow \Pi_M^P\,(P_{n-1})$	▷ Carry out amplitude adaption
5:	$\widehat{(\Psi)_n} \leftarrow \Pi_M^\Psi\,((\Psi)_{n-1})$	
6:		
7:	Compute Π_S^O:	
8:	$O'_n \leftarrow \widehat{(\Psi)_n}/\widehat{P_n}$	▷ Divide for O, i.e. enforce separability
9:	$O_n \leftarrow \Pi_O\,(O'_n)$	▷ and apply constraints
10:		
11:	Compute Π_S^P:	
12:	$P'_n \leftarrow \left(\frac{\widehat{(\Psi)_n}}{O_n} + \widehat{P_n}\right)/2$	▷ Divide for P
13:	$P_n \leftarrow \Pi_P\,(P'_n)$	▷ and apply constraints
14:		
15:	$(\Psi)_n \leftarrow P_n \cdot O_n$	▷ New exit wave
16:	**end for**	

The details of the cross-over update are given in pseudo code in Algorithm 1 in lines 7-13, the corresponding projectors Π_S^O and Π_S^P are detailed below. The operator Π_S^O is used to update the iterate for O. First the fields are separated by division (line 8), enforcing separability. Next, the projector Π_O is used to enforce the constraints on O, i.e. pure, negative phase and support constraint.

$$\Pi_O(\bullet) = \begin{cases} \exp\left(i \cdot \arg\left(\bullet\right)\right) & \text{for pixel} \in S \\ \exp(i \cdot 0) & \text{for pixel} \notin S \vee \arg\left(\bullet\right) > 0 \end{cases} \tag{3}$$

Optics EXPRESS

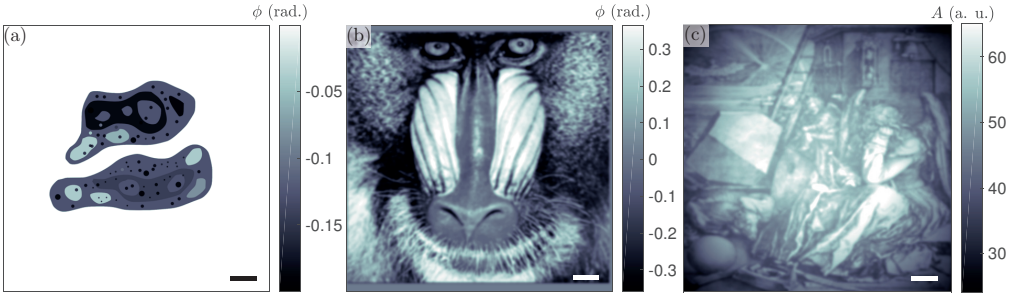

Fig. 4. Phantoms used for the simulation. (a) Phases of the object (pure phase contrast) with $\phi \in [-0.2\ 0]$ rad. (b) Phases of the probe. (c) Amplitudes of the probe. The gray values of the input images are scaled to match phases $\phi \in [-0.4\ 0.4]$ rad and amplitudes $A \in [0.8\ 1.2]$. Amplitude and phase phantom images have been frequency filtered by a Gaussian with FWHM of 5 px. In addition, the amplitudes are multiplied with a Gaussian of 354 px FWHM to simulate an intensity decay. The scale bar indicates 50 px.

Here the support S is assumed to be known, but additional refinements as shrink-wrap can be easily implemented to refine S. In practice, the support is easily generated from the conventional approach of empty beam correction, followed by holographic reconstruction. Note, that any other known constraint on O can be incorporated as well.

Next, P is updated using Π_S^P. The new O_n is used to separate P_n taking also $\widehat{P_n}$ into account (line 12). In a general setting, we can only use the information from $\widehat{P}$ and the division of $\widehat{(\Psi)_n}/O_n$. However, in contrast to the general setting, one often has quite powerful constraints at hand on P, depending on the experimental situation, for example smoothness or small distance with respect to a temporal averaged probe, which would of course further improve convergence. The smoothness of P is generated by the blurring of free-space propagation. It can be estimated from the power spectral density to choose a suitable full width at half maximum (FWHM) value of a Gaussian filter. The filter is respectively applied on the phases and amplitudes of P. Afterwards the filtered amplitudes and phases are recombined. In the presence of strong fluctuations in P multiple recordings $|\mathcal{D}_{\mathrm{Fr}}(P)|^2$ can be combined to an averaged P. By comparing the current iterate of P with the average P it is possible to discriminate variations larger than a given threshold and set these to the average value. These constraints can be additionally enforced as part of Π_P on P'_n (line 13). The updated exit wave $(\Psi)_n$ is calculated by multiplying P_n and O_n (line 15). The Matlab implementation of the algorithm is provided in Code 1 (Ref. [34]).

3. Results

3.1. Simulated data

Figure 4 shows the phantoms used for testing the algorithm. A sketch of two cells (a) [35] serves as pure phase phantom of the object. For the probe phantom, a mandrill test image (b), and Dürer's Melancholia I (c), serve to define phases and amplitudes, respectively. Both images are Gaussian low-pass filtered with a filter of FWHM of 5 px diameter to simulate the smoothing of a probe by propagation. To simulate the finite size of the illumination the amplitudes have been multiplied by a Gaussian window of a FWHM with 354 px. The images have size of 512×512 px^2 embedded in $N_x \times N_y = 2048 \times 2048$ px^2 for propagation. Only the central parts (512×512 px^2) of the images are shown in this and the following figures.

The simulated measurements are depicted in Fig. 5 i.e. (a) $|\mathcal{D}_{\mathrm{Fr}}(\Psi)|^2$ and (b) $|\mathcal{D}_{\mathrm{Fr}}(P)|^2$ for a

Optics EXPRESS

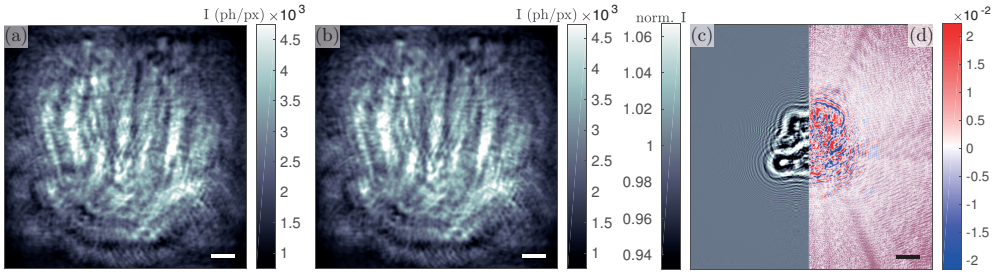

Fig. 5. Simulated input data for the simulations at Fr = 10^{-3} with μ = 200 ph/px, using the phantoms from Fig. 4. The measurements of (a) $|\mathcal{D}_{\mathrm{Fr}}(\Psi)|^2$ and (b) $|\mathcal{D}_{\mathrm{Fr}}(P)|^2$. The scale bar indicates 50 px. (c) The approximated hologram $|\mathcal{D}_{\mathrm{Fr}}(\Psi)|^2/|\mathcal{D}_{\mathrm{Fr}}(P)|^2$. (d) Relative error of (c) to the real hologram $|\mathcal{D}_{\mathrm{Fr}}(O)|^2$. The scale bar indicates 100 px.

Fresnel number of Fr = 10^{-3}. Afterwards, Poissonian noise for a fluence μ = 200 photons/pixel (ph/px) has been added to the measurements. $|\mathcal{D}_{\mathrm{Fr}}(\Psi)|^2$ does not show a visible imprint of the propagated object, due to the comparative small, but for biological specimen reasonable [35] phase shift. The approximated hologram is obtained by the standard flat-field correction i.e. $|\mathcal{D}_{\mathrm{Fr}}(\Psi)|^2/|\mathcal{D}_{\mathrm{Fr}}(P)|^2$ and is shown in (c). This reveals the small contrast range of the imprint. The relative per pixel error of the approximated to the ideal hologram

$$\delta = \frac{(|\mathcal{D}_{\mathrm{Fr}}(\Psi)|^2 \,/\, |\mathcal{D}_{\mathrm{Fr}}(P)|^2 - |\mathcal{D}_{\mathrm{Fr}}(O)|^2)}{|\mathcal{D}_{\mathrm{Fr}}(O)|^2} \tag{4}$$

is shown in (d). The absolute error is $\left(\sum_{\forall \mathrm{pixels}} \left||\mathcal{D}_{\mathrm{Fr}}(\Psi)|^2 \,/\, |\mathcal{D}_{\mathrm{Fr}}(P)|^2 - |\mathcal{D}_{\mathrm{Fr}}(O)|^2\right|^2\right)^{1/2} = 13.9$. The measurements have been then used for two simulations: First we have used the approximated hologram as input for an alternating projection algorithm [35], here we have implemented Relaxed Averaged Alternating Reflections (RAAR) [36]. The iterates of RAAR for the wavefield Ψ under reconstruction are given by

$$\Psi_{n+1} = \frac{\beta_n}{2}\left(R_O(R_M(\Psi_n)) + \Psi_n\right) + (1-\beta_n)P_M(\Psi_n)\,, \tag{5}$$

where $R_{O/M}(\bullet) = 2\Pi_{O/M}(\bullet) - \bullet$ denotes a (mirror) reflection by a given constraint set and n the iteration index. Π_M and Π_O are defined as above in Eq. (1) and Ep. (3), respectively. The parameter β_n controls the relaxation. It follows the function

$$\beta_n = \exp\left(-(n/\beta_s)^3\right)\beta_0 + \left[1 - \exp\left(-(n/\beta_s)^3\right)\right]\beta_{\max}\,, \tag{6}$$

where β_0 denotes the starting value, $\beta_{\max}$ the final value of β_n and β_s the iteration number when the relaxation is switched. This relaxation strategy follows [36] Eq. (37). The parameters have been set to $\beta_0 = 0.99$, $\beta_m = 0.75$, $\beta_s = 500$ for the reconstructions using RAAR.

Second have we used the two simulated holograms as input for d&u. We used the same constraints on O as described in Sec. 2. P is constrained by the magnitude projection and the separability. Additionally a smoothness constraint has been applied in Π_P. Amplitude and phase of P'_n are filtered with a Gaussian with FWHM of 1 px. Both algorithms were executed for 4000 iterations, starting from a amplitude 1, phase 0 initialization over the whole reconstruction area. Figure 6 summarizes the results.

By comparison of (a) and (b), the improved reconstruction quality of d&u is clearly evidenced. The background of (b) shows less distortions and small phase differences are reconstructed with

Optics EXPRESS

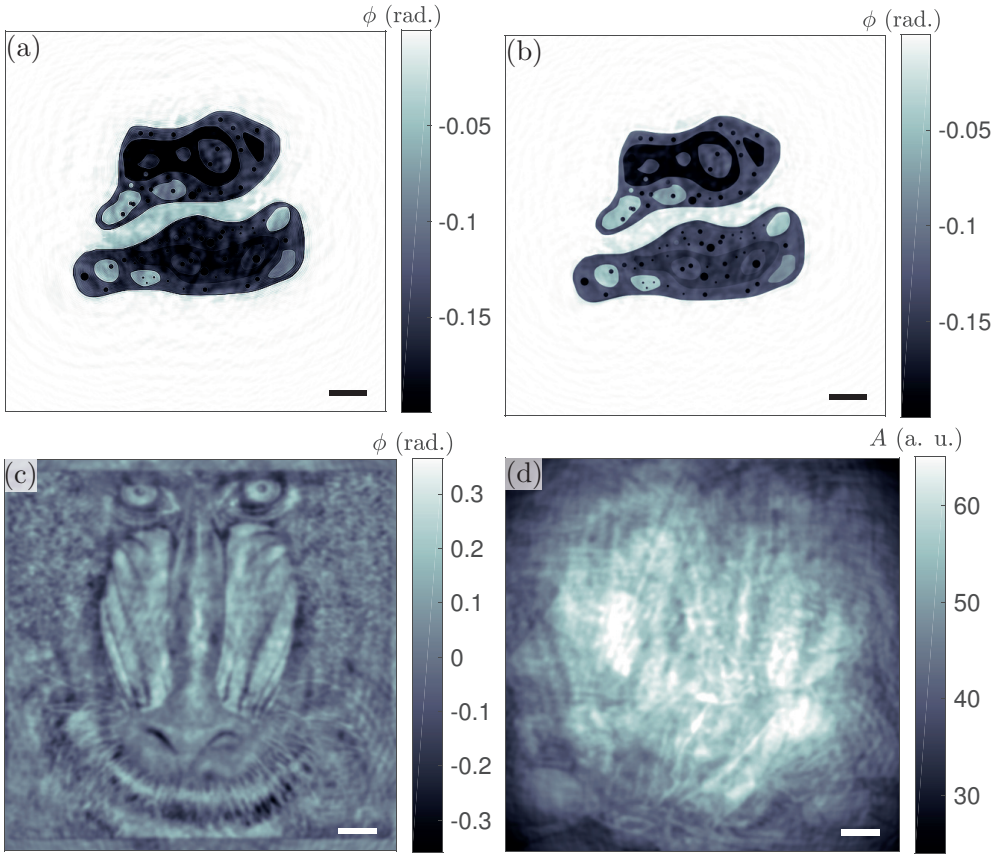

Fig. 6. Results obtained with divide&update for simulated noisy data with $\mu = 200$ ph/px after 4000 iterations. (a) The reconstructed object phases, obtained from conventional flat-field corrected data using RAAR. (b) The reconstructed object obtained from d&u. (c) Phases and (d) amplitudes of the reconstructed probe. The scale bar indicates 50 px.

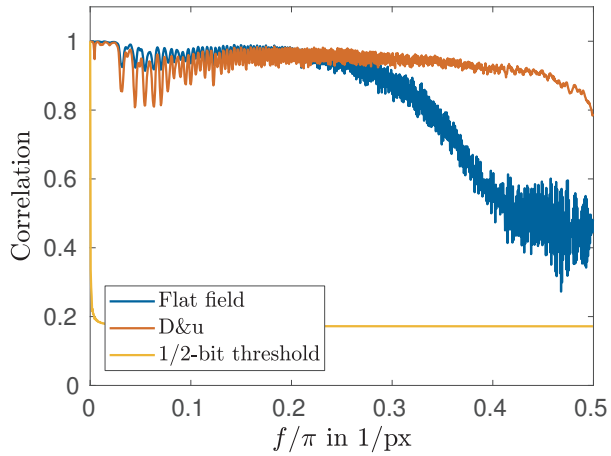

Fig. 7. Fourier ring correlation of the reconstructions of O shown in Fig. 6 with respect to the phantom Fig. 4(a).

Optics EXPRESS

better contrast, see for example the center region of the lower cell. The ringing artifacts at the edges of the object, which are observed in the standard flat-field correction scheme, disappear.

In addition to the object and in contrast to the standard scheme, d&u can recover P, at least to some extent, as shown in Fig. 6(c) and (d). The phases (c) show a good recovery of the edges compared to Fig. 4(b), but the low frequencies seem not recovered as well which is evidenced by the reduced contrast as compared to the original. Further, the amplitudes (d) are not as well recovered as the phases, some larger structures are recognizable as the cube left and the sitting angel on the right. Further below, we will discuss remedies which improve probe reconstruction, by slightly changing the setting. Since only one measurement for P is used and no additional constraints on phase or amplitude, the reconstruction suffers from twin image artifacts and missing spatial frequency information. Figure 7 shows the results for the Fourier ring correlation (FRC) [37, 38] on the object reconstructions of Fig. 6(a) and (b) and the phantom Fig. 4(a). The flat field (blue) and d&u (red) reconstruction do not drop below the 1/2-bit threshold (yellow), this means both reconstructions have resolution down to the pixel level. The FRC yields more insight, it shows that the d&u reconstruction, while slightly lacking for frequencies in the range $[0.02, 0.15]$ 1/px, has a superior recovery of frequencies beyond 0.25 1/px. The normalized Frobenius norm

$$\Delta = \frac{1}{N_x N_y}\left(\sum_{\forall \text{ pixels}} \left|\arg(\text{phantom}) - \arg(\text{reconstruction})\right|^2\right)^{1/2} \tag{7}$$

is for the flat-field reconstruction $\Delta = 4.58 \cdot 10^{-5}$ and for d&u $\Delta = 2.45 \cdot 10^{-5}$.

3.2. Experimental data

In addition to the simulations, we present reconstructions obtained from experimental data, recorded at ESRF beamline ID16a using a photon energy of 17.05 keV, at instrumental settings described in [39]. The object consisted of spheres of different diameters 595 nm (SiO_2), 3 and 7 µm (polysterene). It was placed at a defocus distance of $z_1 = 13.79$ mm. A FReLoN 2k ($N_x \times N_y = 2048 \times 2048$ px^2) detector was used for recording the data with a pixel size of 845 nm, placed at a defocus distance of $z_2 = 435.56$ mm. The exposure time was 1 s, 2 exposures have been acquired, one with and one without object in the beam. The exposures have been corrected for dark current, lens distortions and scintillator impurities. The images have been then normalized by their corresponding mean intensity value. The resulting normalized intensity distributions have been used as input for the reconstruction algorithms. Figure 2 shows the preprocessed input for (a) the measurement $|\mathcal{D}_{\text{Fr}}(\Psi)|^2$, (b) the measurement $|\mathcal{D}_{\text{Fr}}(P)|^2$ and (c) the flat-field correction obtained from (a) divided by (b). The effective object pixel size is 26.7 nm, given by the detector pixel size and the geometric magnification $M = z_2/z_1 \approx 31.5$. After transformation to a parallel beam (effective) geometry using the Fresnel scaling theorem, the (effective) Fresnel number is $\text{Fr} = 7.3 \cdot 10^{-4}$.

Figure 8 shows the reconstruction results after 20000 iterations for different reconstruction schemes applied on the same input data, as shown in Fig. 2. The reconstruction obtained by a standard iterative phase reconstruction algorithm scheme is shown in (a) and (b). As input the flat-field corrected single distance measurement was used, cf. Fig. 2(c). The reconstructions (c) and (d) obtained by d&u used the measurements shown in Fig. 2(a) and (b) as input. The phase retrieval for Fig. 8(a) and (b) was carried out with RAAR, using the same set of constraints (pure phase shifting sample as well as the support constraints) as in the numerical experiment. This is to be compared with the reconstructions of O using d&u, shown in (c) and (d), which both exhibit improved reconstruction quality compared to (a) and (b), in particular an improved suppression of the P induced artifacts stemming from the KB aberrations. Also the resolution is improved, as judged from inspection of the smallest spheres, see also (e) for a zoom on

Optics EXPRESS

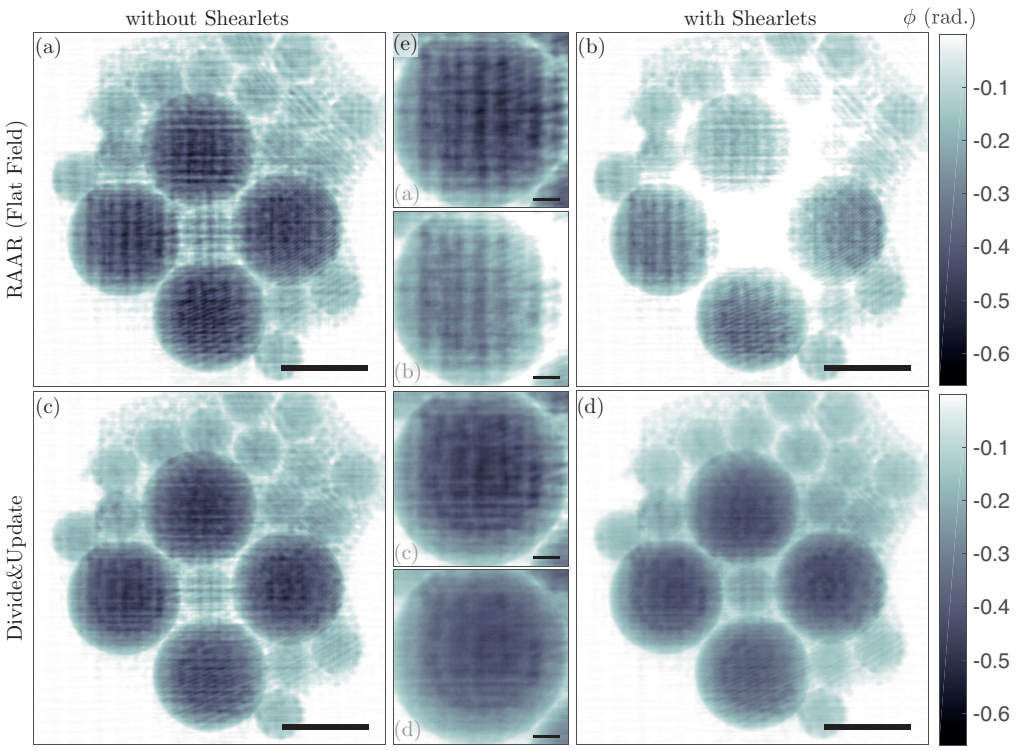

Fig. 8. Object phase reconstructions obtained by different reconstruction schemes applied to the same input data, shown in Fig. 2. (a) Reconstruction obtained by RAAR using the flat-field corrected input data after 20000 iterations. (b) same as (a) with shearlet supression. (c) The d&u reconstruction shows significantly reduced artifacts. (d) same as (c) with shearlet supression. All reconstructions shown are after 20000 iterations and the color bar applies to all panels. The scale bar indicates 5 μm for (a) to (d). (e) Detail on the left large sphere for (a) to (d) from top to bottom, respectively. The scale bar indicates 1 μm.

the left of the large spheres. All reconstructions shown impose the same constraints on O, i.e. combined support and pure-phase constraint (cf. Eq. 3). In addition for (c) and (d) the physically correct formulation of the separation of complex valued wavefields instead of the flawed flat-field division [12, 13] is used. In the reconstruction of (b) and (d), an additional constraint in form of a shearlet suppression was applied in Π_S^O which for (d) further enhanced the reconstruction quality. For (b) the same set of shearlets has been suppressed as in (d) but with a negative effect on reconstruction quality. For this constraint, a shearlet decomposition [40–42] was used to identify components which appear both in P and the reconstructed O. These shared components are then removed from the object, as detailed in App. B. In (d) even the small spheres beneath the large sphere on the left become distinguishable. Still we note remaining structures which can be accounted to drift in P, i.e. inconsistency due to the fact that the object and empty beam recordings were not simultaneous, as proposed in the FEL illumination scheme sketched in Fig. 1. All reconstruction parameters are tabulated in Tab. 1.

The reconstructed phases and amplitudes of the probe are shown in Fig. 9 (a) and (b), respectively. The probe's phase does not show a visible imprint of the object, contrary to the object where we observe remains of the probe. The amplitudes show no imprint, but we observe a decay of intensity towards the edge of the field of view, as we expect from a finitely extended

Optics EXPRESS

Table 1. Summary of the parameters for the experiment.

Parameter	Value
Detector pixel size	845 nm
z_1	13.79 mm
z_2	435.56 mm
Magnification	31.5
Effective pixel size	26.7 nm
Fr	$7.3 \cdot 10^{-4}$
Iterations(simulation)	4000
Iterations(experiment)	20000

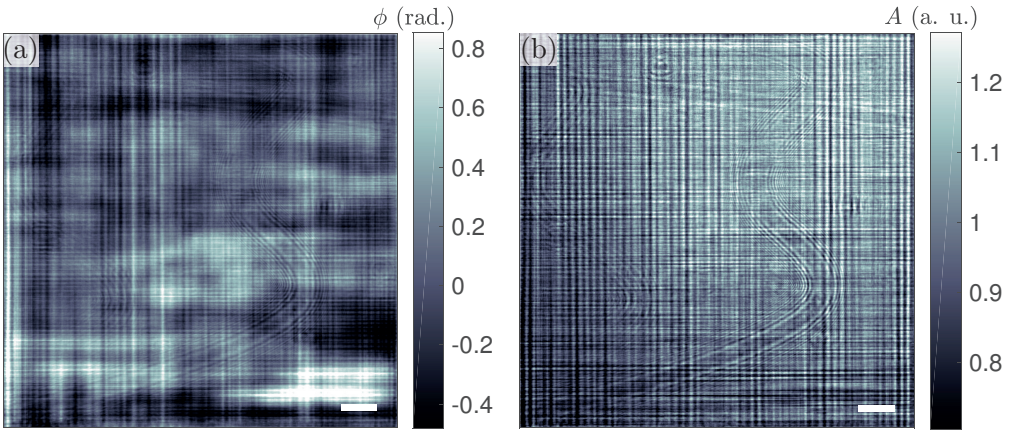

Fig. 9. Reconstructed probe P, obtained simultaneously with the object shown in Fig. 8(c). Phases and amplitudes are shown in (a) and (b), respectively. The scale bar indicates in all panels 5 μm.

illumination. Overall the separation of P and O works very well. The reconstruction was carried out as in the case for simulated data. However, a larger number of iterations is required, compared to simulated data. Inspection of the object reconstruction after 4000 iterations shows that the object has 'holes' which fill up with more iterations. Therefore a much higher number of iterations $n_{max} = 20000$ was used. The convergence rate can further be quantified by the error metric $\Delta_{\mathcal{X}}$ as a function of iteration n, as shown in Fig. 10. $\Delta_{\mathcal{X}}$ calculates the per pixel error of the reconstructed intensity $I_{\mathcal{X}}$ with respect to the measurements $M_{\mathcal{X}}$,

$$\Delta_{\mathcal{X}} = \sum_{\text{all pixels}} |\, I_{\mathcal{X}} - M_{\mathcal{X}}|^2 \,/N. \tag{8}$$

4. Discussion and outlook

Both simulation and experiment validate the proposed approach for simultaneous probe and object reconstruction in the optical near field, using a miniumum of data, i.e. one recording with and one without the object (empty beam). In practice the two recordings can be acquired sequentially, as in the present experimental realisation, or simultaneously, if a second semi-transparent detector screen is used in front of the object, see Fig. 1. This is to be compared to established near-field ptychographic schemes, which are based on

Optics EXPRESS

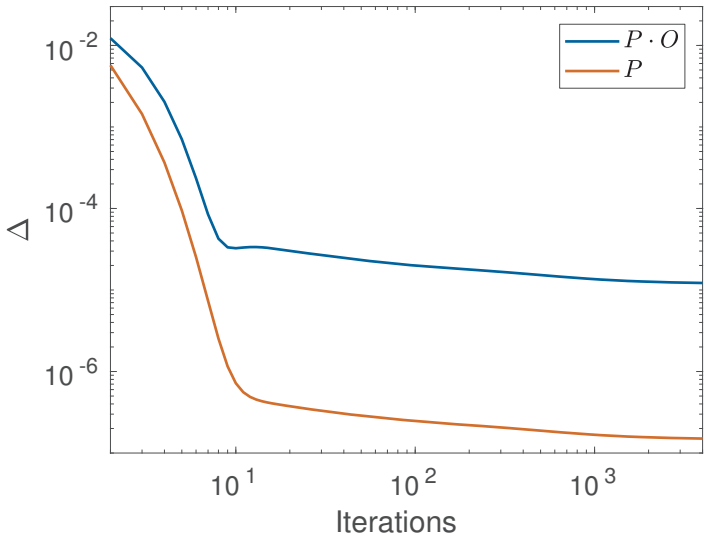

Fig. 10. Error measure Δ as function of the iteration number for the exit wave's Ψ (blue) and probes P (red) reconstructed intensity.

lateral [43, 44] and/or longitudinal translations of the object [22, 45]. Hence, the standard approaches require sequential recordings and significantly more input data. In particular, they are neither compatible with time-dependent imaging nor with non-stationary illumination (probe). Unwanted probe fluctuations are particularly problematic in FEL imaging using stochastic SASE pulses, with considerable pulse-to-pulse fluctuations.

The price for relaxing the need of a stationary probe is a stronger set of constraints. Here we have used the constraints of a pure phase object and a support for the object and smoothness for the probe. Additionally we have employed a shearlet decomposition to identify and remove artifacts stemming from the probe. This is not a severe restriction for holography of biological (from cells to tissues) and soft matter samples at the nano scale, since total absorption is significantly reduced compared to macroscopic phase contrast imaging. For example the model protein $H_{50}C_{30}N_9O_{10}S$ [35, 46] has at an energy of 17.5 keV an attenuation coefficient of $1.38{\cdot}10^{-7}$ nm^{-1}.

Further, extended samples could possibly also be used in this scheme if the probe is fully captured by the detector, including the beam tails. Therefore, we anticipate that the presented scheme is ideally suited for single pulse full field FEL imaging even in the presence of strong pulse-to-pulse fluctuations. Using nano-focused illumination and high geometric magnification M as recently realized with SR [17], sub-50 nm resolution and typical FOV in the range of several 10 micrometers are realistic.

Finally, we want to briefly address probe reconstruction. The results of the probe reconstruction shown in Fig. 6 (simulated data) is still quite flawed, in particular concerning the amplitudes. This can be avoided if the empty beam and the object recordings are carried out in two different planes, which is not the actual geometry realized in the present experiment at ID16a, but the geometry proposed in Fig. 1 for future FEL work. As shown by further simulation in App. A, recording P and Ψ in two different planes already stabilizes the reconstruction. We also stress that the Mandrill-Dürer probe is certainly an extreme case and could be replaced by an 'easier' setting with a smooth probe, for example a probe where more constraints can be applied from prior knowledge, e.g. from recording a data stream of typical probe fluctuations. A

Optics EXPRESS

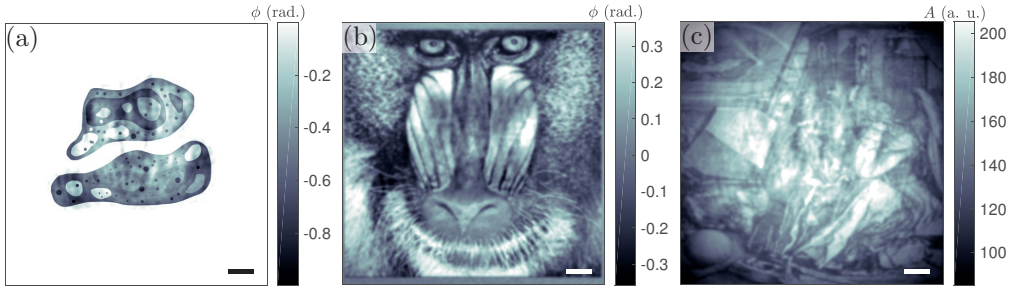

Fig. 11. Reconstructions for parallel acquisition setup. Structure as in Fig. 4. (a) Phases of the reconstructed object. (b, c) reconstructed probe in phase and amplitude, respectively, in the probe's reference plane located at $\mathrm{Fr} = 1 \cdot 10^{-3}$ in front of the object. The scale bar indicates 50 px.

machine learning algorithm could then identify a lower dimensional space of 'allowable' probes. This issue is left for future investigation.

In summary, combination of common constraints with separability of P and O yields a minimalistic implementation of ptychography and a significant improvement in resolution, phase sensitivity and reduced probe artifacts as compared to reconstructions using flat-field corrected data. The divide and update scheme (d&u) presented here could also be extended to far-field imaging (coherent diffractive imaging) in a straightforward way. Finally, we want to point out the advantages of d&u also for the case of imaging with stationary probes. Conventional probe and object retrieval by multi-plane detection or multi-object translations requires substantial recording time. Contrarily, single distance recordings are preferred in particular for tomographic scans. The present scheme reconciles such single distance recordings with proper treatment of an aberrated (non-ideal) probe.

Appendix A: Simulation for parallel data acquisition scheme

The proposed setup for parallel data acquisition Fig. 1 has been validated by simulation. The reference plane for P has been set at $\mathrm{Fr} = -1 \cdot 10^{-3}$ in front of the plane of O. This way we can simulate effects of a propagated probe at the object plane. Starting from the plane of O we have simulated measurements of Ψ for $\mathrm{Fr}_\Psi = 1 \cdot 10^{-3}$ and P for $\mathrm{Fr}_P = -5 \cdot 10^{-3}$ (in front of O). Poissonian noise corresponding to 2000 ph/px has been added to the measurements. Figure 11 shows the reconstructions of O (a) and P (b,c) after 4000 iterations of d&u without shearlet constraint. Inspecting the reconstructions shows, that the amplitudes of P (c) are recovered much better than in Fig. 6. The second measurement distance for P breaks the twin image symmetries(complex conjugates) and eliminates these artifacts. The remaining artifacts in P stem from the incomplete separation of O. Note, a smaller Fr_P yields a better reconstruction of P. The reconstruction of O is spoiled by some low frequency artifacts as compared to Fig. 6. Using shearlets to identify unseparated contributions in O can improve the reconstruction.

Appendix B: Details of the shearlet suppression

For enhancing the reconstruction a shearlet suppression has been applied in each iteration step. The shearlet transformation has been calculated using ShearLab 3D v1.1 [40, 47]. A shearlet system with 4 scales and {1, 1, 2, 2} shears per respective scale. This results in a system redundancy of 49 shearlets. Starting with the reconstruction of O shown in Fig. 8(b) and P in Fig. 9, the phases of these wavefields have been decomposed in the shearlet basis. In order to find the shearlets with the largest contribution, the shearlets intensity, i.e. the sum

Optics EXPRESS

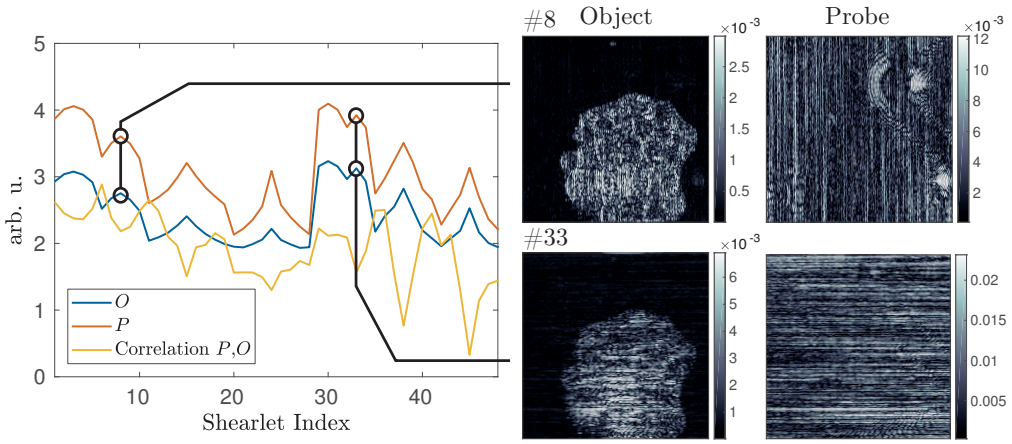

Fig. 12. Shearlet analysis of O and P. (left) The red and blue curve show the intensity of the shearlets as function of the shearlet's index. The yellow curve shows the correlation of the respective shearlet coefficients for P and O. (right) The coefficient matrices of O and P for the shearlets with index #8 and #33.

of the shearlet's coefficients as function of the shearlet index is shown in Fig. 12(left). The blue and red curve show the shearlet's intensities for O and P(left), respectively. These curves have basically the same, but shifted functional form. The shift results from the fact, that we have assumed for $|O(x, y)| = 1$, while P is allowed to have spatially varying intensity values ≥ 1. The sensitivity of the shearlets to structures in the reconstruction is exemplarily shown on the right. To exemplify this, shearlets with large contribution for vertical and horizontal structures are shown, respectively #8 and #33. To gain further inside we have calculated the correlation of O and P for each shearlet coefficient. This has been achieved by using the MATLAB function `norm2xcorr`. The yellow curve shows the correlation of the P and O shearlets, for zero-shift. Certain shearlets show only a weak correlation and visual inspection shows indeed that these are the shearlets describing the horizontal and vertical stripes on different scales in the reconstruction. The first approach, to threshold all shearlets below a certain correlation value yields only poor image quality, since some of the removed shearlets carry important resolution information, e.g #$\{29, 34, 39\}$. After visual inspection, the shearlets S_{VI} with indices #$\{3, 8, 15, 30, 31, 33, 38\}$ have been suppressed, which has yielded the best reconstruction shown in Fig. 8(c). The supression has been carried out by multiplying the whole coefficient matrix corresponding to a shearlet by a factor θ, in this case $\theta = 0.8$. The shearlet suppression was applied in each iteration of the reconstruction run for the result shown in Fig. 8(c), providing additional constraint as part of Π_S^O. Contrarily, Figure 13 illustrates the effect of (a) applying the shearlet suppression as mere post-processing image filter compared to (b) incorporating the suppression in the algorithm. This shows that the additional computational effort yields an improved reconstruction.

This scheme is a first approach to incorporate the shearlet decomposition in phase retrieval to enhance separability of P and O it can be further extended: The shearlet components extracted from O can be 'transplanted' in the corresponding coefficients of P. The suppression parameter θ can be relaxed, in order to boost artifact removal at the beginning of the reconstruction and later to find a stable solution. Multiplying the complete coefficient matrix with θ is rather harsh, since the shearlets give highly localized information, one could look for areas in the image, where the variation is strong and apply there locally the suppression. Finally we want to note, that the separation of P and O shows similarities to image separation problems [40, 48].

Optics EXPRESS

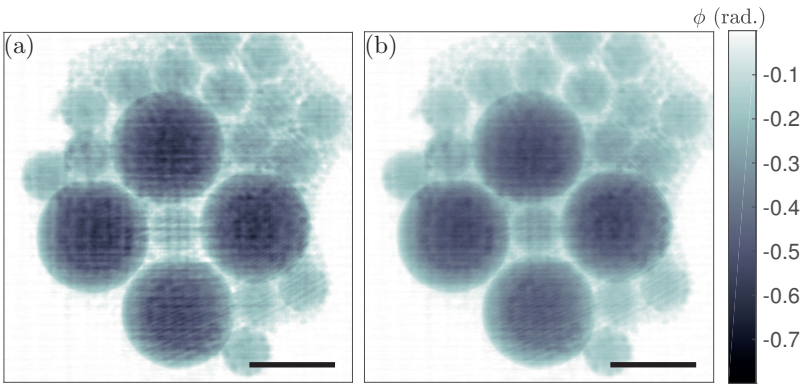

Fig. 13. Effect of shearlet suppression. (a) shows the effect of the shearlet suppression applied on the object's reconstruction shown in Fig. 8(b). (b) the same as Fig. 8(c), where the shearlet suppression has been applied as part of Π_S^O in each iteration. The scale bar indicates in all panels 5 µm.

Funding

Deutsche Forschungsgemeinschaft (DFG) (SFB 755); Bundesministerium für Bildung und Forschung (BMBF) (05K16MGB).

Acknowledgments

We thank Mareike Töpperwien and Peter Cloetens for invaluable help during the beam time. We thank Aike Ruhlandt and Jan-David Nicolas for fruitful discussions. We thank Jan Goeman for keeping the number crunching machines up and running.